RESEARCH ARTICLE

NANO · MICRO small
www.small-journal.com

Metabolism-Regulating Nanozyme System for Advanced Nanocatalytic Cancer Therapy

Chang Liu, Xiaoyu Xu, Yongyang Chen, Miao Yin, Ermei Mäkilä, Wenhui Zhou, Wenmei Su, and Hongbo Zhang**

Nanocatalytic therapy, an emerging approach in cancer treatment, utilizes nanomaterials to initiate enzyme-mimetic catalytic reactions within tumors, inducing tumor-suppressive effects. However, the targeted and selective catalysis within tumor cells is challenging yet critical for minimizing the adverse effects. The distinctive reliance of tumor cells on glycolysis generates abundant lactate, influencing the tumor's pH, which can be manipulated to selectively activate nanozymatic catalysis. Herein, small interfering ribonucleic acid (siRNA) targeting lactate transporter-mediated efflux is encapsulated within the iron-based metal–organic framework (FeMOF) and specifically delivered to tumor cells through cell membrane coating. This approach traps lactate within the cell, swiftly acidifying the tumor cytoplasm and creating an environment for boosting the catalysis of the FeMOF nanozyme. The nanozyme generates hydroxyl radical (·OH) in the reversed acidic environment, using endogenous hydrogen peroxide (H_2O_2) produced by mitochondria as a substrate. The induced cytoplasmic acidification disrupts calcium homeostasis, leading to mitochondrial calcium overload, resulting in mitochondrial dysfunction and subsequent tumor cell death. Additionally, the tumor microenvironment is also remodeled, inhibiting migration and invasion, thus preventing metastasis. This groundbreaking strategy combines metabolic regulation with nanozyme catalysis in a toxic drug-free approach for tumor treatment, holding promise for future clinical applications.

1. Introduction

Nanozymes are an emerging class of enzyme mimetics or artificial enzymes based on nanomaterials and follow similar enzymatic kinetics and mechanisms as natural enzymes under physiological conditions.[1] Nanozymes have high enzyme activity which is tunable via size control, doping, and surface modification, are highly stable, easy to scale up, and with low cost.[2] These advantages make them superior to natural enzymes or traditional enzyme mimetics in practical applications. In recent years, nanozymes have been widely used in biomedical applications, including biosensors, antibacterial and anticancer therapies.[3] Notably, the iron-mediated Fenton reaction has attracted particular interest in the nanocatalytic reactions of various nanozymes,[4–6] which hold a highly potent advanced oxidation procedure for antitumor therapy due to its ability to catalyze larger amounts of endogenous metabolites into highly reactive oxygen species (ROS), thereby delivering controlled multi-level damage to specific

C. Liu, Y. Chen, M. Yin, W. Su, H. Zhang
Department of Pulmonary Oncology
Affiliated Hospital of Guangdong Medical University
Zhanjiang 524001, China
E-mail: suwenmei123@hotmail.com; hongbo.zhang@abo.fi

C. Liu, Y. Chen, M. Yin, W. Su, H. Zhang
Guangdong Provincial Key Laboratory of Autophagy and Major Chronic Non-communicable Diseases
Affiliated Hospital of Guangdong Medical University
Zhanjiang 524001, China

C. Liu, X. Xu, W. Zhou, H. Zhang
Pharmaceutical Sciences Laboratory
Faculty of Science and Engineering
Åbo Akademi University
Turku 20520, Finland

The ORCID identification number(s) for the author(s) of this article can be found under https://doi.org/10.1002/smll.202307794

DOI: 10.1002/smll.202307794

X. Xu, W. Zhou, H. Zhang
Turku Bioscience Centre
University of Turku and Åbo Akademi University
Turku 20520, Finland

X. Xu
ENT Institute and Department of Otorhinolaryngology
Eye & ENT Hospital
State Key Laboratory of Medical Neurobiology
Institutes of Biomedical Sciences
Fudan University
Shanghai 200031, China

E. Mäkilä
Industrial Physics Laboratory
Department of Physics and Astronomy
University of Turku
Turku 20014, Finland

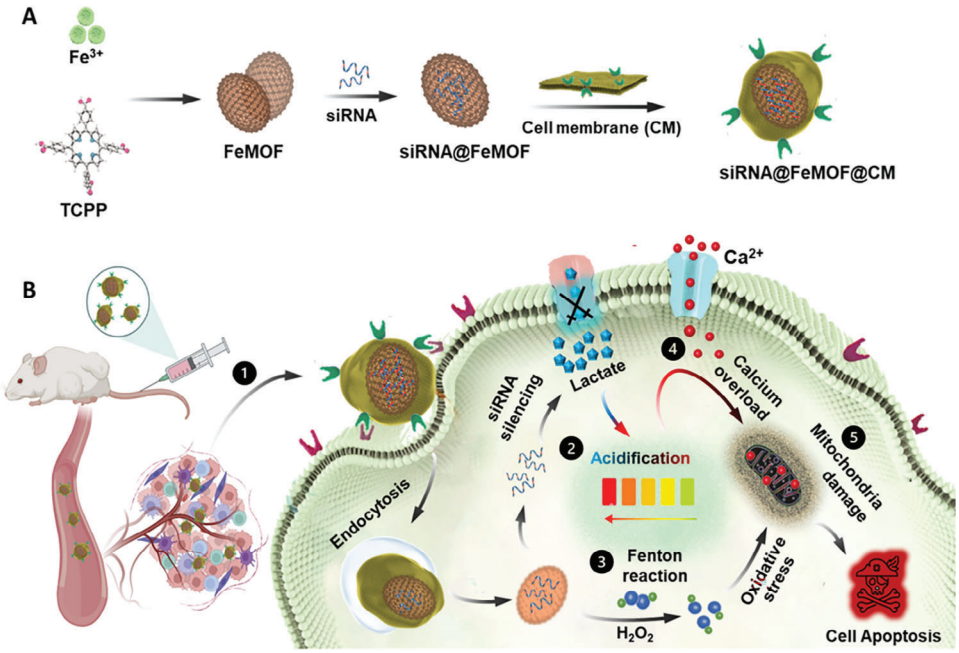

Scheme 1. Schematic illustration of FeMOF nanozyme for multimodal synergistic lung cancer therapy. A) Synthesis of the cancer-cell-membrane-coated self-assembled nanoFeMOFs siRNA@FeMOF@CM. B) The corresponding anticancer mechanism of the siRNA@FeMOF@CM nanozyme. ①The functionalization of the nanoFeMOFs with cancer cell membranes (CM) facilitates their active internalization into tumor cells. ②Upon escaping from lysosomes, the released siRNA from FeMOF@CM inhibits MCT4-mediated lactate efflux in tumor cells through gene silencing, trapping lactate within the intracellular compartment, and rapidly acidifying the tumor cytoplasm. ③The acidification further strengthens the pH-responsive Fenton-like reactions of FeMOF, generating a large quantity of hydroxyl radicals (·OH) in close proximity to the mitochondria. ④Simultaneously, the intracellular acidification induces calcium influx, leading to calcium overload within the mitochondria. ⑤Consequently, the abundant ·OH and calcium overload synergistically inflict dual damage on mitochondria, ultimately inducing cell death.

targets, such as organelles critical for tumor cell development,[7–10] which is an approach that has the desirable specificity and efficacy in terms of its antitumor capacity. Nevertheless, with traditional Fenton homogeneous nanozymes, Fe(II)/Fe(III) ions are hardly recovered and are limited to acidic environments.[11,12] Therefore, regulatory strategies capable of modulating tumor cell metabolism are required in order to achieve selective activation of nanocatalysis for clinical applications.

Glycolysis is a prevalent metabolic characteristic of tumor cells, resulting in the production of substantial amounts of lactate in the cytoplasm, which significantly affects intracellular and extracellular pH levels.[13–17] To adapt to glycolysis-induced lactate accumulation, tumor cells often upregulate the expression of various lactate transporters, such as monocarboxylate transporter 4 (MCT4), which expels lactate from the cytoplasm to the extracellular space.[18,19] This process helps maintain the intracellular pH of tumor cells at a mildly alkaline level ≈7.4 while acidifying the tumor microenvironment to a pH of 6.8, thus promoting tumor cell growth and enhancing stemness and metastasis.[20–22] Regulation of endogenous MCT4-mediated lactate transport by siRNA could reverse the pH gradient inside and outside the tumor cells, allowing for selective implementation of Fenton-like antitumor approaches in the intracellular milieu and potentially other therapeutic effects. Given the pivotal role of siRNA-mediated pH regulation, it has become imperative to develop a nanocarrier with inherent catalytic capabilities to facilitate effective siRNA delivery.

Recently, metal–organic frameworks (MOFs) are a class of porous materials consisting of metal cations/clusters that are interconnected by bridging organic building blocks,[23,24] which has led to their applications in catalysis, drug delivery, and cancer treatment.[25–29] They have unprecedented porosity and tunability and therefore have the potential to control their function through molecular design. Unlike inorganic porous materials with fixed and unchanging structures,[30,31] MOFs can be modified using a complete toolbox of organic synthesis with pores that can be decorated with catalytic sites. Meanwhile, MOFs are most often crystalline, which allows us to study the distribution of active sites within the framework and also to assess the effect of the framework on the catalytic activity.

In this study, we present a novel core-shell nanoparticle comprised of iron-based metal–organic frameworks (FeMOFs), as illustrated in **Scheme 1**, which are hybrid solids with a periodic network structure composed of iron ions with tetrakis (4-carboxyphenyl) porphyrin (TCPP). The specific textural features of FeMOFs, like the wide distribution of single iron sites, porous structures, and large surface areas, confer them with abundant exposed active sites and favorable access of reactants to active sites, turning them into a promising heterogeneous Fenton-like nanozyme. Benefiting from the superior anti-immune clearance and homologous targeting ability of the coated cell membrane (CM), the synthesized nanozyme can be endocytosed by the cancer cells, which, together with the presence of a site-specific substance (H_2O_2), enables for selective nanozyme therapy specifically targeted to the mitochondria of tumor cells.[32–34] Moreover,

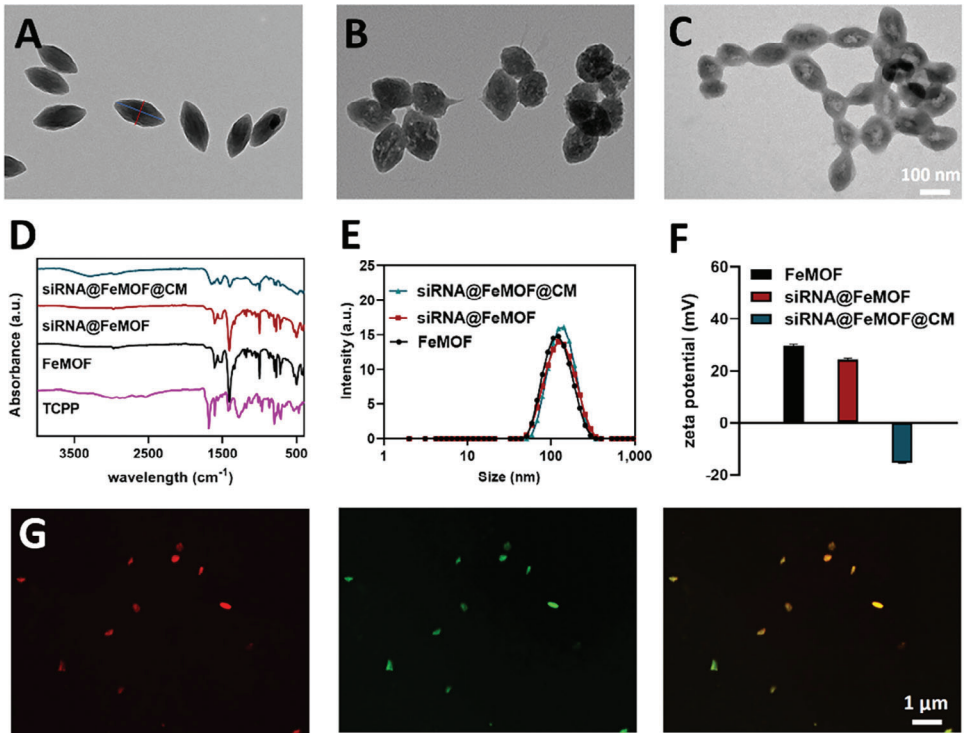

Figure 1. The fabrication and characterization of the nanozyme. TEM images of FeMOF (A), siRNA@FeMOF (B) and siRNA@FeMOF@CM (C). D) FTIR spectra of TCPP, FeMOF, siRNA@FeMOF and siRNA@FeMOF@CM. Hydrodynamic size distribution (E) and zeta potential (F) for FeMOF, siRNA@FeMOF and siRNA@FeMOF@CM in aqueous solution. G) Super-resolution images of FeMOF@CM stained with membrane dye DiO (green). ExCM: 488 nm; ExFeMOF: 561 nm.

FeMOF nanoparticles with tailor-designed porous structures can be used to encapsulate and control the delivery of siRNA, which could provide the protection of the payload from premature leakage, while being sheltered under harsh conditions. Through the lysosome pathway, the released siRNA silences theMCT4gene to inhibit lactate efflux (Figure S1, Supporting Information), causing intracellular retention of lactate and subsequent tumor cytoplasmic acidification. The upregulated H_2O_2, FeMOF, and acidic intracellular environment within the mitochondria promote the heterogeneous Fenton-like response that exacerbates oxidative stress. At the same time, intracellular acidification triggered calcium influx, leading to mitochondrial calcium overload. These combined effects involving various cellular mechanisms contribute to mitochondrial dysfunction and ultimately to tumor cell death. Furthermore, the siRNA-regulated lactate efflux blockade not only exerts a direct therapeutic effect but also neutralizes the acidic tumor microenvironment, inhibiting tumor migration and invasion, thus preventing metastasis. These results shed light on the potential of combining cancer metabolic regulation with MOF-based nanozyme for tumor treatment, providing a novel approach to the exploration of advanced nanocatalytic therapies with improved efficacy, precision, and safety.

2. Results and Discussion

2.1. Preparation and Characterization of the Nanozyme

A novel nanozyme has been developed by utilizing FeMOF due to its pH-responsive catalysis activity, excellent biocompatibility as well as high cargo loading capacity, and multifunctional modification potential. FeMOF was synthesized using a well-established solvothermal method, revealed a fusiform-like structure with an average size of 100 ± 10 nm in length and 50 ± 5 nm in diameter, characterized by transmission electron microscopy (TEM) in **Figure** 1A. The Ar adsorption isotherm shown in Figure S2A (Supporting Information) presents a steep gas uptake at low relative pressures, typical for microporous materials. The apparent specific surface area was estimated with the BET method, indicating the available area of ≈505 ± 9 m^2 g^{-1}, which was beneficial to the formation of the catalytic interface.[35] The density functional theory (DFT) calculations utilizing a zeolite model suggest the pores to be well in the micropore region, with a diameter of 0.5–1 nm, as shown in the Figure S2B (Supporting Information), confirming that the FeMOF were able to accommodate siRNA into the pore and surfaces of FeMOF.[36] The diameter of siRNA@FeMOF and siRNA@FeMOF@CM slightly increased after loading siRNA and modifying with the cancer cell membrane (Figure 1B,C), as also confirmed by scanning transmission electron microscopy (STEM)-based energy-dispersive X-ray spectroscopy (EDX) analysis, which indicated the deposition of siRNA and cell membrane on the nanoparticle surface (Figure S3A, Supporting Information). The preparation and modification of the nanoparticle samples were further validated by changes in Fourier-transform infrared spectroscopy (FTIR), size distribution, and zeta potential (Figure 1D–F). Survey spectra with the main elements observed are shown in Figure S2C (Supporting Information). Core level spectra of Fe 2p show clearly the spin-orbit splitting, along with the

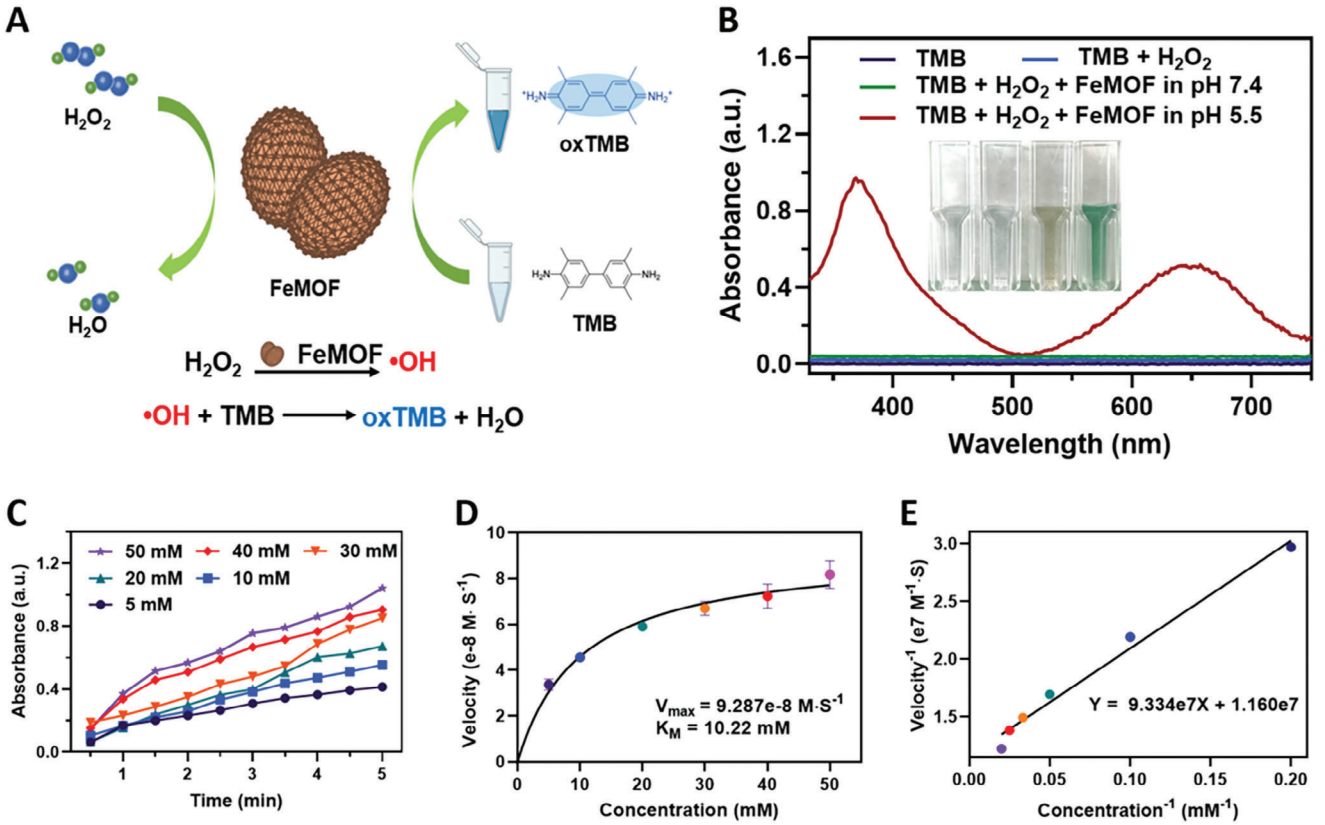

Figure 2. The characterizations of the catalytic performances of the nanozyme. A) Schematic diagram depicting the catalytic process of FeMOF nanozyme. It shows the interaction between FeMOF, H_2O_2, and TMB during the catalytic reaction. B) UV–vis absorption spectra and visual color changes of the catalyzed oxidation of TMB. The spectra and corresponding digital photos show the absorbance changes and color variations of the reaction mixture containing TMB, H_2O_2, and FeMOF at different pH conditions (pH 7.4 and pH 5.5) in phosphate-buffered saline. Insets show the corresponding digital photos of each group. C) Time-dependent absorbance changes at 652 nm. The graph displays the absorbance changes over time at 652 nm, representing the catalyzed oxidation of TMB by FeMOF at various concentrations of H_2O_2 (5, 10, 20, 30, 40, and 50 mM). D) Michaelis-Menten kinetic analysis. The graph presents the relationship between the concentration change rate of TMB (v) and the corresponding concentration of H_2O_2. It allows the determination of kinetic parameters such as the Michaelis-Menten constant (K_M) and the maximal velocity of the reaction (V_{max}). E) Lineweaver-Burk plot. The plot is a graphical representation of the Michaelis-Menten equation using reciprocal values of the concentration change rate of TMB and the concentration of H_2O_2. It enables the calculation of KM and V_{max} for the catalytic reaction of FeMOF with H_2O_2.

broadening of peaks toward higher binding energies (Figure S2D, Supporting Information). With the Fe $2p_{3/2}$ peaks appearing near 711 eV along with an adjacent satellite structure near 718 eV, these results suggest Fe(III) and Fe(II) valence states, as observed in Fenton-like activity.[37] Super-resolution microscopy images demonstrated a good co-localization pattern between FeMOF (red fluorescence from sulfo-Cyanine5.5 NHS ester (Cy5.5)) and the cancer cell membrane (green fluorescence from the stained DiO), confirming the successful formation of the membrane enclosed FeMOF@CM (Figure 1G).[38] This observation was consistent with the X-ray diffraction patterns (XRD) of FeMOF and siRNA@FeMOF@CM, which exhibited identical crystallinity features (Figure S3B, Supporting Information). Furthermore, FeMOF nanozymes showed structural stability after 4 days of incubation at room temperature in neutral pH and serum, which confirms its physicochemical stability in clinical situations (Figure S3C, Supporting Information). The nanozyme was slightly degraded at acidic pH, but this would occur in siRNA-initiated cells and did not affect siRNA delivery or the catalytic ability of FeMOF. According to Figure S3D (Supporting Information), the siRNA loading amount was 85% when the siRNA/FeMOF ratio set as 1:16, which is consistent with the high specific surface area and large porosity of FeMOF and the interaction between siRNA and FeMOF.

2.2. Characterization of the Catalytic Performances of the Nanozyme

To assess the Fenton-like catalytic activity of FeMOF, a commonly used colorimetric method employing 3,3′,5,5′-tetramethylbenzidine (TMB) as a substrate was utilized.[39–41] In the presence of H_2O_2, FeMOF acts as a nanozyme, oxidizing TMB and generating a blue-colored product called oxidized TMB (oxTMB) with distinct absorbances at 370 and 652 nm (**Figure 2A**). The reaction mechanism involves two steps: first, the O—O bond in the H_2O_2 molecule splits, generating ·OH; secondly, ·OH oxidizes TMB to form oxTMB. UV–vis absorption spectroscopy was employed to monitor the formation of oxTMB, and without the presence of FeMOF, no absorbance

was observed (Figure 2B), indicating that no oxidation reaction occurred in the TMB and H_2O_2 mixture. However, when FeMOF was added to the TMB/ H_2O_2 solution (under pH 5.5, which mimics the acidity in the cytoplasm after siRNA treatment), a blue-colored solution with absorbance peaks at 370 and 652 nm emerged, confirming the generation of ·OH by FeMOF and H_2O_2. Conversely, only a small amount of ·OH was generated at pH 7.4, which corresponds to the pH of normal cells. Due to its catalase-like property under neutral or basic pH conditions, FeMOF converted H_2O_2 into harmless oxygen instead of ·OH. The pH-dependence of nanozyme catalyzed ·OH production is beneficial in diminishing its toxicity to normal cells.

To further investigate the catalytic activity of FeMOF nanozyme, the steady-state catalytic kinetics were examined at room temperature in a reaction system comprising FeMOF, TMB, and different concentrations of H_2O_2 (5, 10, 20, 30, 40, and 50 mM) at pH 5.5. The time-dependent changes in absorbance of the reaction solution were monitored at 652 nm by Nanodrop (Figure 2C). For each H_2O_2 concentration, the rate of change in oxTMB concentration (v) was calculated based on the rate of change in absorbance using the Beer–Lambert law, $A = \epsilon lc$ (where A is the absorbance, ϵ is the molar absorbance coefficient, l is the path length, and c is the molar concentration), with l = 10 mm and ϵ of 39000 M^{-1} cm^{-1} for oxTMB. The rate of change in TMB concentration was plotted against the corresponding H_2O_2 concentrations, and the data fit the Michaelis–Menten equation (Figure 2D), represented as:

$$v_0 = V_{max}[S] / (K_M + [S]) \quad (1)$$

where v_0 represents the initial reaction rate, V_{max} is the maximum velocity of the reaction, [S] denotes the substrate concentration, and K_M is the Michaelis–Menten constant. The Michaelis–Menten equation provides a quantitative description of the relationship between the rate of substrate conversion and the concentration of the substrate. The V_{max} value reflects the catalytic activity of the enzyme. By rearranging the original Michaelis-Menten equation, we obtain the form shown below:

$$1/v_0 = K_M/V_{max}[S] + 1/V_{max} \quad (2)$$

Based on the Lineweaver–Burk plot (Figure 2E), the K_M and V_{max} values for the catalytic reaction by FeMOF with H_2O_2 as the substrate were determined. The K_M value represents the substrate concentration at which the reaction rate is half of the maximum, while the V_{max} value represents the maximum reaction rate achievable under saturating substrate conditions. In this case, the K_M and V_{max} values were found to be 10.22 mM and 9.287×10^{-8} M s^{-1}, respectively. These values provide quantitative information about the catalytic efficiency and affinity of FeMOF toward H_2O_2 as a substrate.

2.3. Tumor Targeting and Lysosomal Escape Capability of the Nanozyme

To assess the tumor-specificity of the nanozyme, we labeled them with Cy5.5 and examined their uptake by different cell lines, including A549 and MCF-10A, using confocal microscopy. The results demonstrated the enhanced uptake of FeMOF@CM by A549 cells compared to pristine FeMOF, as indicated by the significantly higher Cy5.5 fluorescence observed in the FeMOF@CM group (**Figure 3A**). Quantitative flow cytometry analysis further confirmed the increased fluorescence in A549 cells treated with FeMOF@CM compared to FeMOF over time (Figure 3B). In contrast, both FeMOF and FeMOF@CM exhibited low levels of Cy5.5 fluorescence in MCF-10A cells (Figure S4A, Supporting Information), indicating the tumor specificity of the FeMOF nanozyme.[42] These findings were supported by quantitative flow cytometric analysis (Figure S4B, Supporting Information). To exert its therapeutic effects, the nanozyme needs to interact with specific intracellular components, which requires it to escape from the lysosome to avoid being degraded and eliminated. As shown in Figure 3C, with the help of the CM, FeMOF@CM-treated A549 cells exhibited separated green and red fluorescence after 6 h, indicating that the nanozymes successfully escaped from the lysosomes. The co-localizations of FeMOF@CM and endo/lysosome were analyzed by calculating the Pearson's correlation (Figure S4C, Supporting Information). The results showed that the Pearson's correlation reached the maximum value at ≈4 h ≈81.2% after treating A549 cells with Cy5.5-FeMOF@CM, revealing that the nanoparticles mainly located in the endo/lysosome after entering the cells within ≈4 h. After that, Cy5.5-FeMOF@CM successfully escaped from the endo/lysosome, because the Pearson's correlation began to drop to 29.7% at 6 h after treatment. These observations emphasize the importance of efficient lysosomal escape for the nanozyme to fulfill its therapeutic action.[43,44]

2.4. Metabolic Modulation of Tumor pH-Induced Oxidative Stress and Ca^{2+} Influx

Following the treatment with siRNA-incorporated nanozyme, the expression of MCT4 was effectively suppressed, as evidenced by Western blot results (Figure S5A, Supporting Information), leading to changes in extracellular pH (Figure S5B, Supporting Information). In the nanozyme-treated cells, the intracellular lactate concentration increased, as indicated by the enhanced fluorescence of the pHrodo Green AM intracellular pH indicator, which is sensitive to higher acidity (**Figure 4A**; Figure S5C, Supporting Information). Severe intracellular acidification was observed in A549 cells treated with siRNA@FeMOF or siRNA@FeMOF@CM, while the cytosolic pH of siRNA or FeMOF-treated cells remained unchanged.

The Fenton-like catalytic capability of the nanozyme was further investigated in vitro. Fluorescence imaging using a hydroxyl radical assay kit revealed strong green fluorescence in treated with siRNA@FeMOF@CM, indicating efficient hydroxyl radical generation (Figure 4B; Figure S6, Supporting Information).[45] In contrast, only a modest increase in fluorescence was observed in the FeMOF and siRNA@FeMOF groups, due to the lack of an acidic environment for the catalytic reaction. These results confirmed the necessity of pH modulation to improve the catalytic efficacy. Abnormal

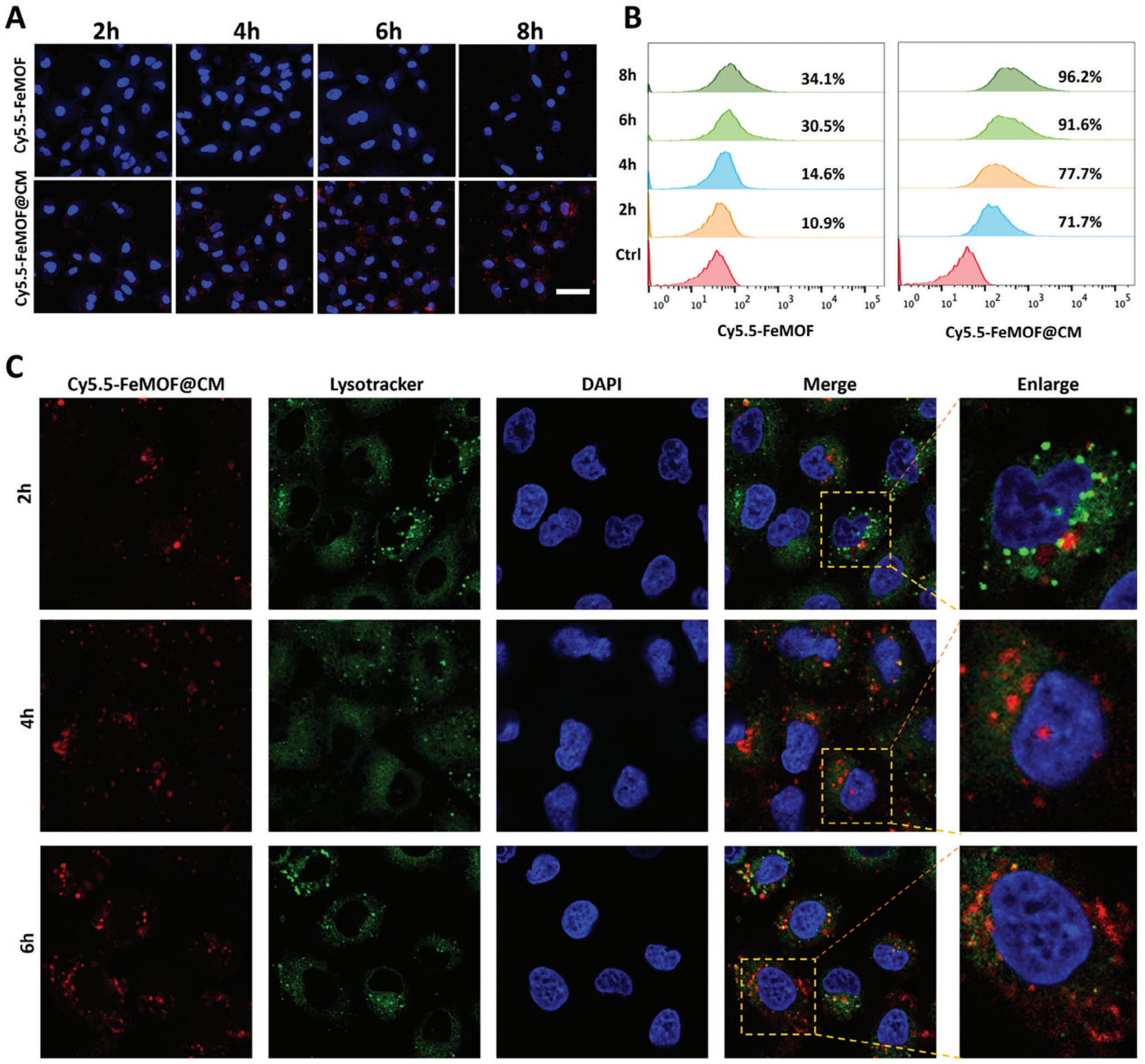

Figure 3. Targeted endocytosis and endosomal escape analysis of the nanozyme in cancer cells. A) CLSM images of A549 cells after treatment with FeMOF and FeMOF@CM for different time intervals (2, 4, 6, and 8 h, scale bar = 20 μm). B) Flow cytometry analysis of A549 cells after incubation with FeMOF and FeMOF@CM. The fluorescence intensity of the cells is measured, and A549 cells without any treatment are used as a blank control group. C) CLSM images of A549 cells cultured with FeMOF@CM for different time intervals (2, 4, and 6 h). The red fluorescence represents Cy5.5 loaded by the nanoparticles, the green fluorescence represents lysosomes labeled with Lysotracker staining, and the nuclei are stained blue with DAPI (scale bar = 10 μm).

intracellular acidity often leads to an imbalance in intracellular calcium levels. The variation of intracellular calcium levels in A549 cells was studied using Fluo-3 as a fluorescent calcium probe (Figure 4C; Figure S7, Supporting Information). There was no significant increase in intracellular calcium concentration as a result of treatment with siRNA or FeMOF. However, in cells incubated with siRNA@FeMOF@CM, which benefited from excellent protection and efficient endocytosis by the cancer cell membrane, a clear difference in cytoplasmic calcium levels was observed, with siRNA@FeMOF@CM-internalized cells displaying stronger fluorescence compared to siRNA@FeMOF-internalized cells. This acidification-enabled upregulation of intracellular calcium levels also led to an increase in mitochondrial calcium levels. The siRNA@FeMOF@CM group exhibited higher expression levels of mitochondrial calcium uniporter (MCU) compared to the siRNA@FeMOF group (Figure 4D; Figure S8, Supporting Information)[46,47]

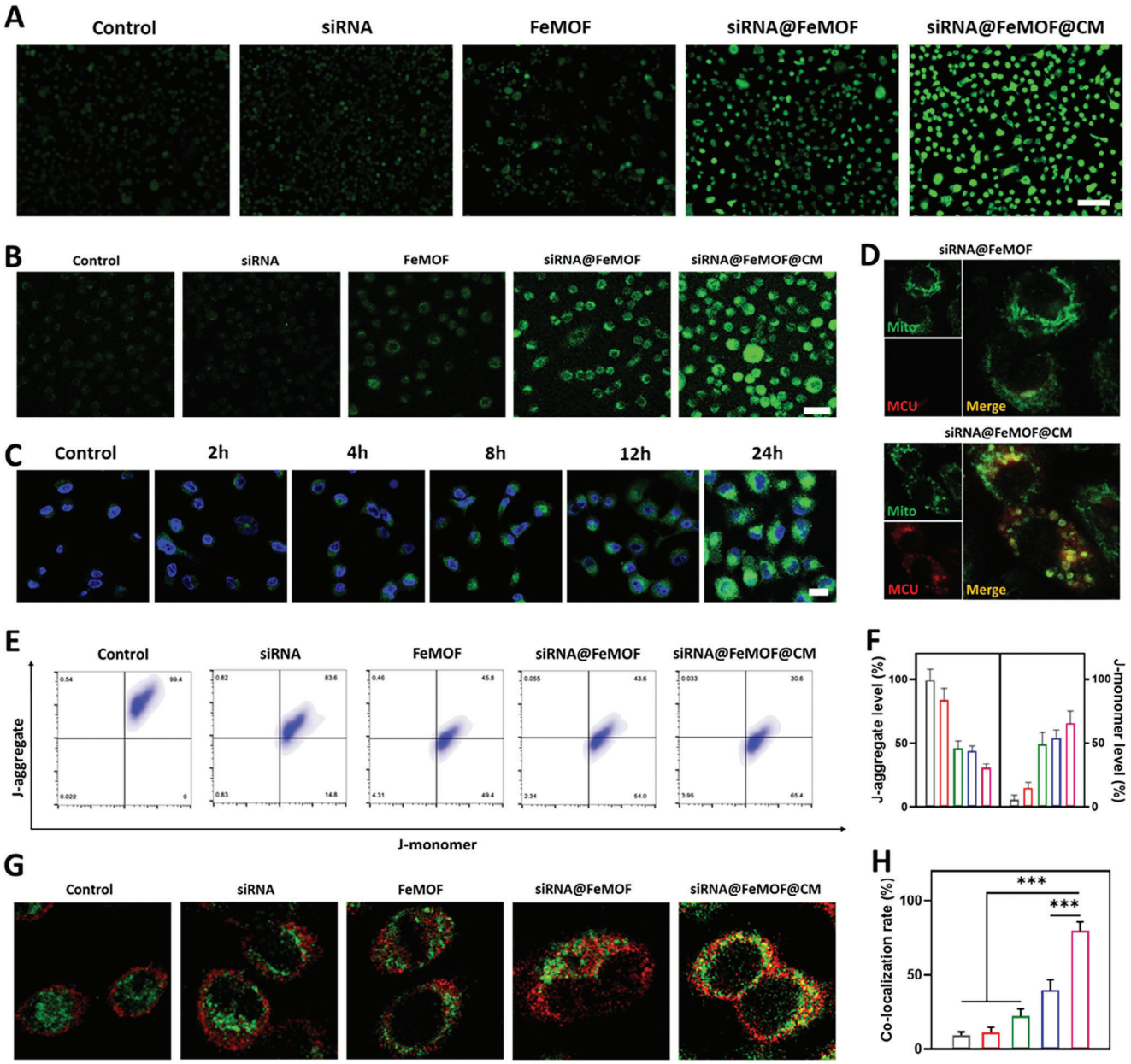

Figure 4. The metabolic modulation of intracellular pH and the synergistic effect of oxidative stress and calcium influx on mitochondria under various treatments. A) Confocal Laser Scanning Microscopy (CLSM) images showing the analysis of pH values in different treatment groups (Control, siRNA, FeMOF, siRNA@FeMOF, and siRNA@FeMOF@CM). The greener the cell, the more acidic it is. The scale bar represents 50 μm. B) Detection of reactive oxygen species (ROS) production in A549 cytoplasm using DCFH-DA (2",7"-dichlorofluorescein diacetate) with different treatments. Green fluorescence indicates the presence of ROS. The scale bar represents 20 μm. C) CLSM images showing calcium influx in the siRNA@FeMOF@CM group at different time periods. Green fluorescence indicates the presence of calcium. The scale bar represents 20 μm. D) CLSM images display the expression of mitochondrial calcium uniporter (MCU) in mitochondria. Green fluorescence represents mitochondria, while red fluorescence represents MCU expression. E) Analysis of mitochondrial membrane potential in A549 cells treated with different groups, measured using flow cytometry. F) Quantitative analysis of J-aggregate and J-monomer in various treatments. The graph illustrates the relative amounts of J-aggregate and J-monomer formed. G) CLSM images showing the expression of cyclophilin D (Cyp D) in A549 cells treated with different groups. Green fluorescence represents mitochondria, while red fluorescence represents Cyp D expression. H) The co-localization rate of the nanozyme with mitochondria in different groups, was quantitatively analyzed. The data are presented as mean values ± standard deviation (SD) with $n = 3$ biologically independent samples. Statistical analysis was performed using one-way ANOVA to determine the significance.

2.5. Synergistic Enhancement of Mitochondrial Damage

Having demonstrated the dual effects of siRNA-regulated intracellular acidification promoted ·OH production and calcium overload in mitochondria, their synergistic impact on mitochondrial damage was also studied. Taking into account that mitochondrial membrane potential (MMP) is usually sensitive to both the accumulation of ROS and calcium overload in mitochondria,[48] the MMP of A549 cells following different treatments was assessed using JC-1 dye as an indicator, which typically forms aggregates on normal mitochondrial membranes with relatively high MMP, while it exists as monomers on abnormal mitochondrial membrane with low MMP. The flow cytometry analysis in Figure 4E,F revealed that the siRNA@FeMOF@CM group exhibited the lowest proportion of aggregates (30.6%) and the highest proportion of monomers (65.4%) compared to the other groups, indicating an abnormal MMP status.

To further verify mitochondrial abnormalities, the translocation of the cyclophilin D (Cyp D) protein from the cytoplasm to mitochondria was evaluated, as it is associated with the formation of the mitochondrial permeability transition pore complex.[49] Mitochondria were labeled with MitoTracker Green (as green fluorescence), and the translocation of immunostained Cyp D (as red fluorescence) was assessed. As anticipated, a significant transfer of Cyp D molecules to the mitochondria was observed in the siRNA@FeMOF@CM group (Figure 4G), with a colocalization rate of up to 72.1% (Figure 4H), considerably higher than in the other groups. Overall, the results unequivocally confirmed that the most potent mitochondrial impairment was induced by siRNA@FeMOF@CM, which was attributed not only to the improved endocytosis but also to the synergistic effect of oxidative stress and calcium overload.

2.6. In Vitro Cytotoxicity and Tumor Metastasis Inhibition by Nanozyme

We further evaluated the cytotoxic effects of the nanozyme on tumor cells. As shown in Figure S9A (Supporting Information), there is no obvious therapeutic effect observed in the siRNA or FeMOF groups. It is shown that siRNA@FeMOF exhibited a partial anticancer effect, indicating that FeMOF played a certain protective effect on siRNA and activated the catalytic ability of FeMOF by siRNA-mediated acidic pH. With the CM coating, siRNA@FeMOF@CM exhibited remarkable concentration-dependent cytotoxicity against A549 cells, which implies that active targeting, siRNA acidification, and FeMOF-catalysed binding can effectively destroy cancer cells, which was roughly estimated to be ≈26.3% at 48 h. This result was verified by flow cytometry analysis and cell live/death imaging (**Figure** 5A,B), where the siRNA@FeMOF@CM group had the highest percentage of apoptosis at 60% and the most marked cell death. In contrast, the cytotoxic effect of the nanocarrier alone was remarkably reduced in A549 cells, with a low ratio of cell apoptosis of ≈18% and unapparent cell death according to the WST-1 assay and cell live/death imaging. Furthermore, Western blot analysis was performed to clarify the mechanism of cell damage induced by the FeMOF nanozyme. As shown in Figure S9B (Supporting Information), siRNA@FeMOF@CM treatment substantially decreased the expression of the anti-apoptotic proteins Bcl-xL and Mcl-1, which ultimately led to the activation of the apoptotic executioner Caspase 3. These western blot results indicate that the FeMOF nanozyme induces cell death through the induction of apoptosis, which is consistent with the Fenton therapy of iron-based nanozymes. By blocking lactate efflux through siRNA inhibition, the tumor microenvironment could be modulated, resulting in a complementary therapeutic effect. The migration ability of A549 cells was significantly depressed by treatment with siRNA@FeMOF or siRNA@FeMOF@CM according to the cell scratching assay in Figure S10 (Supporting Information). The relative scratch area of the treated group remained at 76.8%, while that of the control group was only 29.1%, indicating that cell migration was strongly inhibited. The transwell cell migration assay also supported the findings of cell scratch assays showing that the siRNA-incorporated nanozyme could effectively inhibit tumor cell migration (Figure 5C). The inhibition of tumor cell motility and invasiveness induced by treatment after incubating the A549 cells with siRNA@FeMOF@CM was also evidenced by a reduction in cancer cell stemness, in which the CD44 levels in the siRNA@FeMOF@CM group has decreased by 24.4% compared to the control group according to flow cytometric analysis (Figure 5D). The characterization of CD44 expression was also validated by the sphere formation assay, since the siRNA-loaded nanozyme significantly minimized the formation of tumor sphere (Figure 5E; Figure S11, Supporting Information), demonstrating their ability to effectively inhibit the self-renewal of cancer stem cells. Western blot analysis revealed that the nanozyme also inhibited the expression of important tumor metastasis-related markers, such as matrix metalloproteinase-2 (MMP-2) and vascular endothelial growth factor (VEGF), further illustrating its anti-metastatic purpose by changing the pH of the tumor microenvironment (Figure S9B, Supporting Information). These findings highlight the potential of siRNA@FeMOF@CM in inhibiting tumor cell migration, invasiveness, cancer stemness, and metastasis-associated marker expression, thereby suggesting its therapeutic benefits in remodeling the tumor microenvironment.[50,51]

2.7. Combinational Treatment In Vivo

Subsequently, to determine whether FeMOF nanozyme could target tumor tissue and to visualize their biodistribution, an in vivo fluorescence imaging experiments were conducted on A549 tumor-bearing mice after 6, 12, and 24 h tail vein injection of siRNA@FeMOF and siRNA@FeMOF@CM nanoparticles (labeled with Cy5.5). As shown in **Figure** 6A, the fluorescence signal was significantly enhanced in the siRNA@FeMOF@CM group compared to the siRNA@FeMOF group, indicating the accumulation of nanozymes at the tumor site, which was most evident at 24 h. This accumulation is attributed to enhanced permeability and retention (EPR) effects, as well as the improved cell membrane-mediated active targeting. Further sectioning of tumors and organs from mice, fluorescence imaging also revealed that siRNA@FeMOF@CM group had the strongest fluorescence intensity in the tumors and significantly less enrichment in the liver than in the siRNA@FeMOF group, with no significant accumulation in other normal organs (Figure 6B). This difference

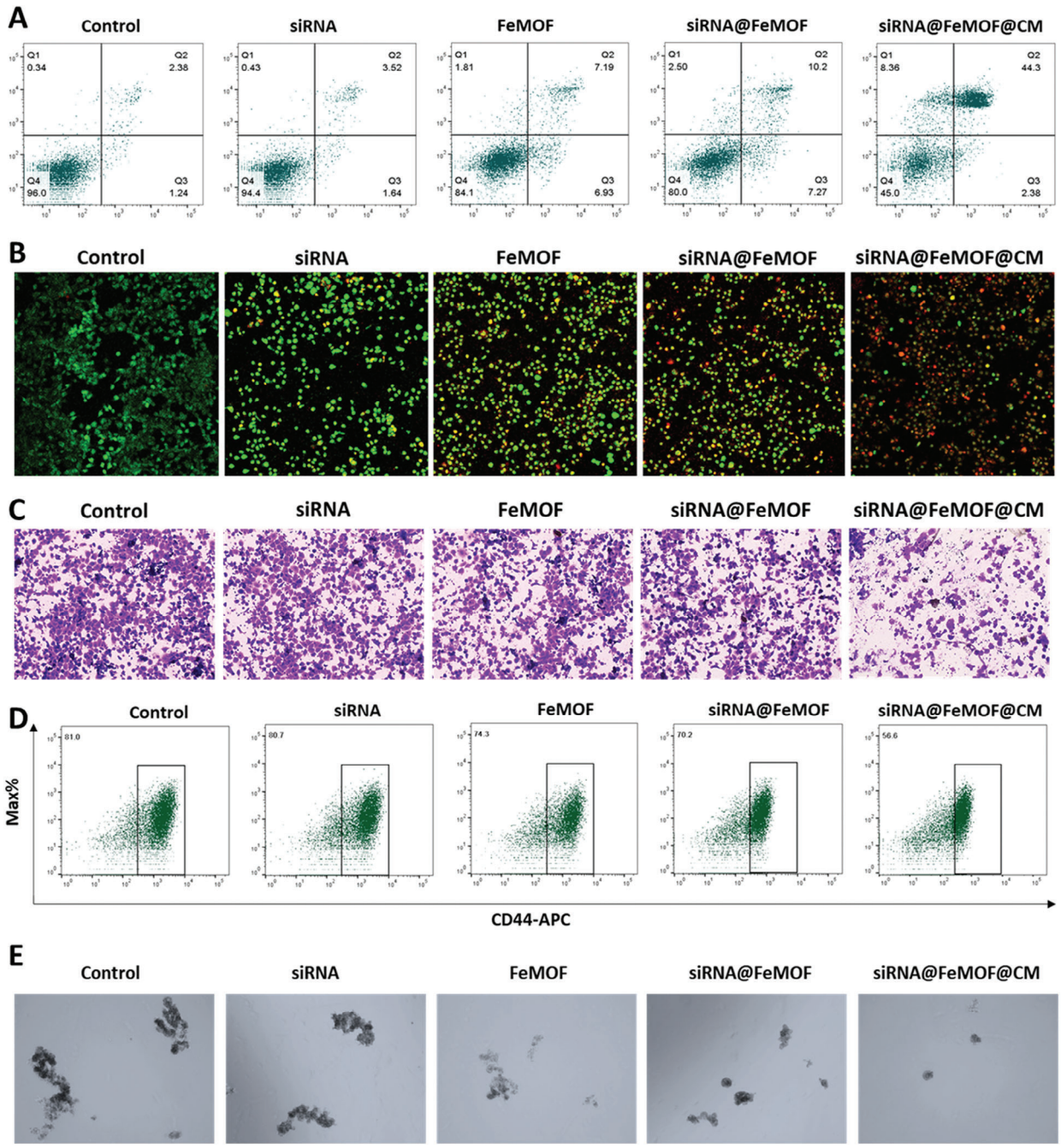

Figure 5. The evaluation of the treatments on cell apoptosis, viability, invasiveness, and stemness. A) Flow cytometric analysis of apoptosis levels in A549 cells treated with control, siRNA, FeMOF, siRNA@FeMOF, and siRNA@FeMOF@CM. B) Live/dead cell images of A549 cells after treatment under different incubation conditions. Red fluorescence indicates dead cells, while green fluorescence represents living cells. C) Transwell invasion assay of A549 tumor cells after treatment with control, siRNA, FeMOF, siRNA@FeMOF, and siRNA@FeMOF@CM, evaluating their invasive potential. D) Flow cytometric analysis of the expression level of the cancer stem cell marker CD44 in A549 cells after treatment with control, siRNA, FeMOF, siRNA@FeMOF, and siRNA@FeMOF@CM. E) Tumor sphere formation assay of A549 cells after treatment with control, siRNA, FeMOF, siRNA@FeMOF, and siRNA@FeMOF@CM, assessing their ability to form tumor spheres.

should be due to the rapid clearance by the immune system and the avoidance of nonspecific uptake.[52,53] These results suggest that siRNA@FeMOF@CM NPs can also promote targeted accumulation of siRNA and FeMOFs at tumor sites, improve the efficiency and specificity of drug utilization, and reduce the toxicity of enrichment in other organs in vivo. The study also investigated the impact of the treatment on tumor tissue pH in A549 tumor-bearing mice using the pH probe. There was no significant effect of treatment with siRNA or siRNA@FeMOF on the extracellular pH of the tumor, which remained ≈6.8.

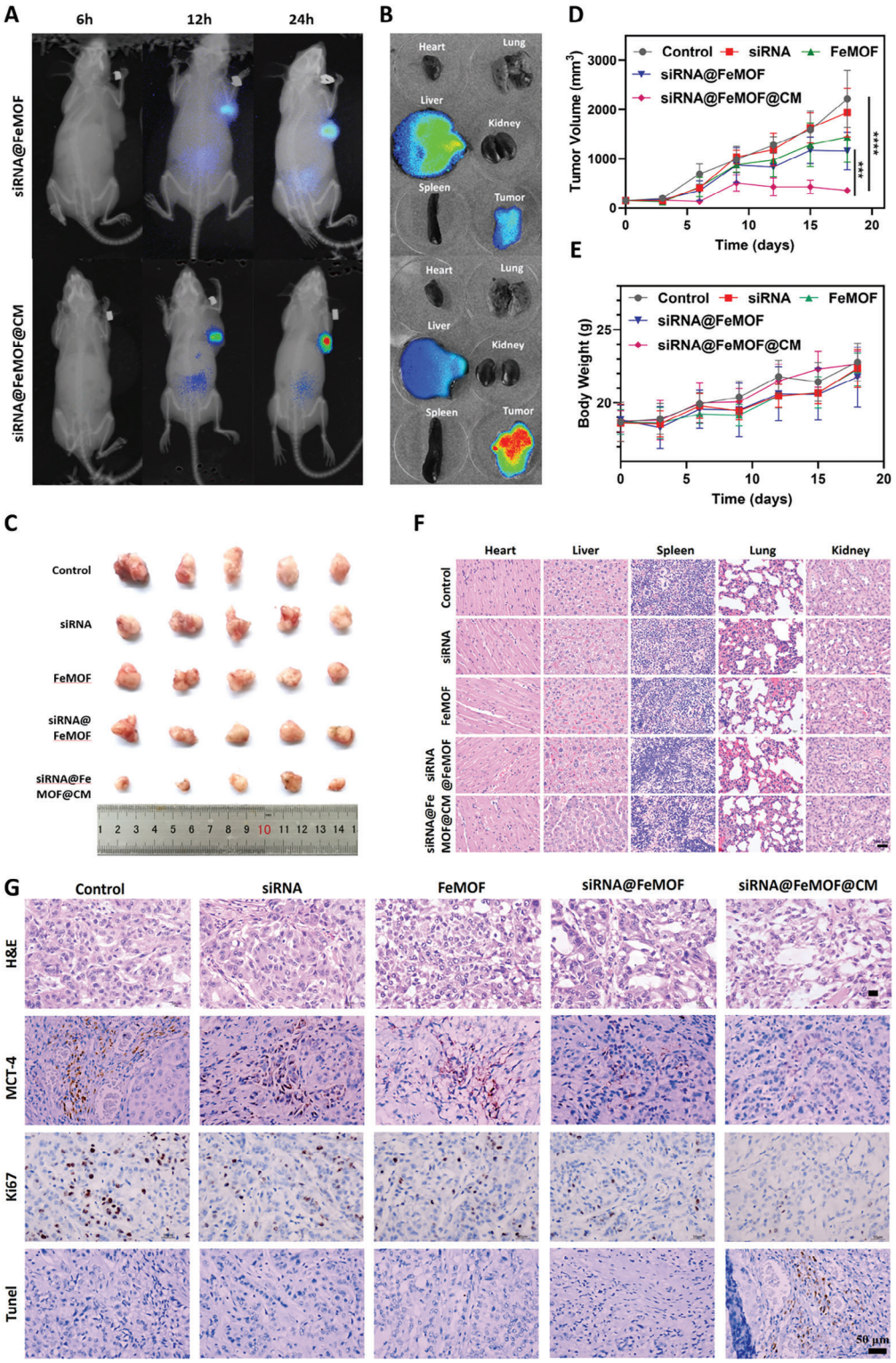

Figure 6. In vivo biodistribution of the nanozyme and antitumor effects in tumor-bearing mice under different treatment groups. A) In vivo fluorescence images of A549 tumor-bearing mice after intravenous injection of siRNA@FeMOF and siRNA@FeMOF@CM, respectively. B) The fluorescence images of the sacrificed mouse tissues, including heart, liver, spleen, lung, kidneys, and tumor at 24 h after intravenous injection of siRNA@FeMOF and siRNA@FeMOF@CM. C) Photographs of the stripped tumors from the sacrificed mouse on the 18th day after administration. D) Tumor volume growth curves and E) the body weight of mice among the different treatment groups. F) The morphology of sectioned organs from the nude mice model in the five groups via H&E staining (scale bar = 200 μm). G) H&E, MCT-4, Ki67, and Tunel staining of sliced tumor tissues after different treatments (scale bar = 50 μm).

However, the application of siRNA@FeMOF@CM caused a noticeable decrease in tumor tissue acidity, leading to an increase in mean pH to 7.2 (Figure S12, Supporting Information). The resulting acidification-induced calcium influx was also verified in tumor tissue as shown in Figure S13 (Supporting Information). These results suggest that the siRNA-incorporated nanozyme can specifically regulate tumor pH and calcium level in vivo, potentially contributing to its therapeutic effects.

The tumor inhibition effects of the nanozyme were also evaluated in A549 tumor-bearing mice. Tumor size measurements revealed that siRNA alone had minimal inhibitory effects on tumor growth throughout the treatment period. In contrast, treatment with siRNA@FeMOF@CM led to a potent suppression of tumor growth (Figure 6C). This effect can be attributed to the acidity-dependent ·OH production mediated by siRNA.[54] FeMOF alone exhibited limited tumor inhibition, mainly due to its low catalytic efficacy under normal conditions. Also, the tumor volume curve was consistent with the result displayed in the photos, indicating that synergistic damage to mitochondria has the best therapeutic outcome (Figure 6D). Furthermore, there were no apparent difference in body weight of the mice after treatment with different groups, indicating their tolerability (Figure 6E). The histological inspections of vital organ tissues did not reveal any traces of treatment-induced damage, supporting the biocompatibility and biosafety of the nanozyme under clinically relevant conditions (Figure 6F). These results suggest that siRNA@FeMOF@CM has strong antitumor effects while maintaining good biocompatibility and safety.

To further assess the antitumor ability in vivo, immunohistochemical assays were performed on tumor tissues, to test the key markers that related to tumor growth. As shown in Figure 6G, the MCT-4 expression level of tumor tissues was first examined. Compared to the PBS group, the staining results showed that MCT-4 intensity was reduced in the siRNA@FeMOF group, and lowest in the siRNA@FeMOF@CM group. Tunel signal, a biomarker associated with apoptosis, was significantly increased in siRNA@FeMOF@CM treated mice. The signal representing the proliferation-associated biomarker Ki67 was obviously decreased in siRNA@FeMOF treated mice, especially in siRNA@FeMOF@CM treated groups. All of these results demonstrated that siRNA@FeMOF@CM can efficiently inhibit the tumor growth in vivo, and that better inhibition can be achieved by a combination of oxidative pressure and calcium overload.

3. Conclusion

In summary, our innovative approach combines metabolic regulation with nanozymes catalysis for advanced anticancer therapy. The heterogeneous Fenton-like FeMOF-based nanozyme not only selectively responds to catalytic initiation environments but also serves as a porous nanomaterial for the encapsulation and delivery of siRNA. In general, the combination of the nanozyme with siRNA inhibits lactate efflux from glycolytic tumor cells, leading to intracellular acidification and fostering an environment conducive to FeMOF catalysis. The elevated H_2O_2 in the mitochondria, acting as an endogenous catalytic substrate, coupled with cytoplasmic acidification, initiate a Fenton-like reaction of FeMOF, generating targeted hydroxyl radicals in the mitochondria for specific antitumor efficacy. In addition, the induced acidification disrupts calcium homeostasis, causing calcium influx and mitochondrial calcium overload, amplifying the antitumor effects by inflicting further damage to the mitochondria. Meanwhile, metabolic modulation also regulates the tumor microenvironment, effectively inhibiting tumor cell metastasis. Importantly, the potential adverse effects are mitigated, as the nanozyme has no significant toxic effects on normal cells at neutral/alkaline pH. In essence, our metabolic modulation strategy offers the possibility to rationally regulate tumor cell function, paving the way for synergistic modulation of state-of-the-art MOF-based Fenton-like nanozymes to enhance the efficacy and safety of antitumor therapies.

4. Experimental Section

Experimental Details can be found in Supporting Information.

Supporting Information

Supporting Information is available from the Wiley Online Library or from the author.

Acknowledgements

C.L., X.X., and Y.C. contributed equally to this work. Electron microscopy samples were processed and analyzed in the Electron Microscopy Laboratory, University of Turku; Confocal Imaging/Flow cytometry was performed at the Cell Imaging and Cytometry core at Turku Bioscience Centre, which is supported by Biocenter Finland. The authors acknowledge the Materials Research Infrastructure (MARI) at the Department of Physics and Astronomy, University of Turku for access and support with the XPS facilities and thank Anastassios Papageorgiou at the Univesity of Turku for providing support for XRD analysis. This work was supported in part by the National Natural Science Foundation of China (NSFC) (82073388, 82201287), the Natural Outstanding Youth Fund of Guangdong Province (2022B1515020090), Guangdong Provincial Key Laboratory of Autophagy and Major Chronic Non-communicable Diseases (2022B1212030003), the Affiliated Hospital of Guangdong Medical University Clinical Research Program (LCYJ2020B005), China Postdoctoral Science Foundation (2021M700830), Research Fellow (353146), project (347897), Solutions for Health Profile (336355), InFLAMES Flagship (337531) grants from Academy of Finland, Finland China Food and Health International Pilot Project funded by the Finnish Ministry of Education and Culture.

Conflict of Interest

The authors declare no conflict of interest.

Data Availability Statement

The data that support the findings of this study are available in the supplementary material of this article.

Keywords

calcium overload, metabolism regulation, mitochondrial damages, nanozyme catalysis, oxidative stress

Received: September 7, 2023
Revised: December 17, 2023
Published online:

[1] L. Gao, X. Yan, *Sci. China Life Sci.* **2016**, *59*, 400.
[2] L. Gao, K. Fan, X. Yan, *Theranostics* **2017**, *7*, 3207.
[3] X. Wang, Y. Hu, H. Wei, *Inorg. Chem. Front.* **2016**, *3*, 41.
[4] H. Lin, Y. Chen, J. Shi, *Chem. Soc. Rev.* **2018**, *47*, 1938.
[5] Z. Y. Shen, J. B. Song, B. C. Yung, Z. J. Zhou, A. G. Wu, X. Y. Chen, *Adv. Mater.* **2018**, *30*, 1704007.
[6] S. Lee, E. Tak, J. Lee, M. Rashid, M. P. Murphy, J. Ha, S. S. Kim, *Cell Res.* **2011**, *21*, 817.
[7] P. Zheng, B. Ding, R. Shi, Z. Jiang, W. Xu, G. Li, J. Ding, X. Chen, *Adv. Mater.* **2021**, *33*, 2007426.
[8] D. Hanahan, R. A. Weinberg, *Cell* **2011**, *144*, 646.
[9] O. Ubah, H. Wallace, *Curr. Pharm. Des.* **2014**, *20*, 201.
[10] Y. Wang, X. Ma, W. Zhou, C. Liu, H. Zhang, *Smart Medicine* **2022**, *1*, e20220013.
[11] S. Navalon, A. Dhakshinamoorthy, M. Alvaro, H. Garcia, *Chem. Rev.* **2014**, *114*, 6179.
[12] M. Vilve, A. Hirvonen, M. Sillanpää, *J. Hazard. Mater.* **2009**, *164*, 1468.
[13] T. Cascone, J. A. Mckenzie, R. M. Mbofung, S. Punt, Z. Wang, C. Xu, L. J. Williams, Z. Wang, C. A. Bristow, A. Carugo, M. D. Peoples, L. Li, T. Karpinets, L. Huang, S. Malu, C. Creasy, S. E. Leahey, J. Chen, Y. Chen, H. Pelicano, C. Bernatchez, Y. N. V. Gopal, T. P. Heffernan, J. Hu, J. Wang, R. N. Amaria, L. A. Garraway, P. Huang, P. Yang, I. I. Wistuba, et al., *Cell Metab.* **2018**, *27*, 977.
[14] S. Vasaikar, C. Huang, X. Wang, V. A. Petyuk, S. R. Savage, B. Wen, Y. Dou, Y. Zhang, Z. Shi, O. A. Arshad, M. A. Gritsenko, L. J. Zimmerman, J. E. McDermott, T. R. Clauss, R. J. Moore, R. Zhao, M. E. Monroe, Y. T. Wang, M. C. Chambers, R. J. C. Slebos, K. S. Lau, Q. Mo, L. Ding, M. Ellis, M. Thiagarajan, C. R. Kinsinger, H. Rodriguez, R. D. Smith, K. D. Rodland, D. C. Liebler, et al., *Cell* **2019**, *177*, 1035.
[15] P. S. Gonzalez, J. O'prey, S. Cardaci, V. J. A. Barthet, J.-I. Sakamaki, F. Beaumatin, A. Roseweir, D. M. Gay, G. Mackay, G. Malviya, E. Kania, S. Ritchie, A. D. Baudot, B. Zunino, A. Mrowinska, C. Nixon, D. Ennis, A. Hoyle, D. Millan, I. A. Mcneish, O. J. Sansom, J. Edwards, K. M. Ryan, *Nature* **2018**, *563*, 719.
[16] S. Morioka, J. S. A. Perry, M. H. Raymond, C. B. Medina, Y. Zhu, L. Zhao, V. Serbulea, S. Onengut-Gumuscu, N. Leitinger, S. Kucenas, J. C. Rathmell, L. Makowski, K. S. Ravichandran, *Nature* **2018**, *563*, 714.
[17] R. T. Netea-Maier, J. W. A. Smit, M. G. Netea, *Cancer Lett* **2018**, *413*, 102.
[18] Y. Liu, X. Ji, W. W. L. Tong, D. Askhatova, T. Yang, H. Cheng, Y. Wang, J. Shi, *Angew. Chem. Int. Ed. Engl.* **2018**, *57*, 1510.
[19] D. Benjamin, D. Robay, S. K. Hindupur, J. Pohlmann, M. Colombi, M. Y. El-Shemerly, S.-M. Maira, C. Moroni, H. A. Lane, M. N. Hall, *Cell Rep.* **2018**, *25*, 3047.
[20] Z. E. Walton, C. H. Patel, R. C. Brooks, Y. Yu, A. Ibrahim-Hashim, M. Riddle, A. Porcu, T. Jiang, B. L. Ecker, F. Tameire, C. Koumenis, A. T. Weeraratna, D. K. Welsh, R. Gillies, J. C. Alwine, L. Zhang, J. D. Powell, C. V. Dang, *Cell* **2018**, *174*, 72.
[21] S. R. Pillai, M. Damaghi, Y. Marunaka, E. P. Spugnini, S. Fais, R. J. Gillies, *Cancer Metastasis Rev.* **2019**, *38*, 205.
[22] S. Damgaci, A. Ibrahim-Hashim, P. M. Enriquez-Navas, S. Pilon-Thomas, A. Guvenis, R. J. Gillies, *Immunology* **2018**, *154*, 354.
[23] X. Li, J. Yu, Z. Lu, J. Duan, H. C. Fry, D. J. Gosztola, K. Maindan, S. S. Rajasree, P. Deria, *J. Am. Chem. Soc.* **2021**, *143*, 15286.
[24] M. Zhang, B. Wang, P.-J. Wu, J.-Z. Qi, Y. Xu, J.-F. Zhang, X. Zhang, *Nanomicro Lett.* **2021**, *13*, 56.
[25] Y. Zhang, F. Wang, C. Liu, Z. Wang, L. Kang, Y. Huang, K. Dong, J. Ren, X. Qu, *ACS Nano.* **2018**, *12*, 651.
[26] R. Cheng, L. Jiang, H. Gao, Z. Liu, E. Mäkilä, S. Wang, Q. Saiding, L. Xiang, X. Tang, M. Shi, J. Liu, L. Pang, J. Salonen, J. Hirvonen, H. Zhang, W. Cui, B. Shen, H. A. Santos, *Adv. Mater.* **2022**, *34*, 2203915.
[27] X. Xu, C. Liu, S. Wang, E. Mäkilä, J. Wang, O. Koivisto, J. Zhou, J. M. Rosenholm, Y. Shu, H. Zhang, *Nanoscale* **2022**, *14*, 15832.
[28] C. Liu, X. Xu, O. Koivisto, W. Zhou, G. Jacquemet, J. M. Rosenholm, H. Zhang, *Nanoscale* **2021**, *13*, 16525.
[29] C. Liu, X. Xu, W. Cui, H. Zhang, *Engineered Regeneration* **2021**, *2*, 105.
[30] R. A. Mustafa, P. Parkkila, J. M. Rosenholm, H. Zhang, T. Viitala, *Smart Medicine* **2023**, *2*, e20230012.
[31] X. Xu, S. Wang, Y. Shu, H. Zhang, *Smart Materials in Medicine* **2021**, *2*, 350.
[32] Z. Chai, D. Ran, L. Lu, C. Zhan, H. Ruan, X. Hu, C. Xie, K. Jiang, J. Li, J. Zhou, J. Wang, Y. Zhang, R. H. Fang, L. Zhang, W. Lu, *ACS Nano* **2019**, *13*, 5591.
[33] Y. Jiang, N. Krishnan, J. Zhou, S. Chekuri, X. Wei, A. V. Kroll, C. L. Yu, Y. Duan, W. Gao, R. H. Fang, L. Zhang, *Adv. Mater.* **2020**, *32*, 2001808.
[34] C.-M. J. Hu, R. H. Fang, K.-C. Wang, B. T. Luk, S. Thamphiwatana, D. Dehaini, P. Nguyen, P. Angsantikul, C. H. Wen, A. V. Kroll, C. Carpenter, M. Ramesh, V. Qu, S. H. Patel, J. Zhu, W. Shi, F. M. Hofman, T. C. Chen, W. Gao, K. Zhang, S. Chien, L. Zhang, *Nature* **2015**, *526*, 118.
[35] L. Cui, J. Wu, J. Li, H. Ju, *Anal. Chem.* **2015**, *87*, 10635.
[36] Y. Ding, H. Xu, C. Xu, Z. R. Tong, S. T. Zhang, Y. Bai, Y. N. Chen, Q. H. Xu, L. Z. Zhou, H. Ding, Z. Q. Sun, S. Yan, Z. W. Mao, W. L. Wang, *Adv. Sci.* **2020**, *7*, e20230012.
[37] L. Liang, L.-L. Yang, W. Wang, C. Ji, L. Zhang, Y. Jia, Y. Chen, X. Wang, J. Tan, Z.-J. Sun, Q. Yuan, W. Tan, *Adv. Mater.* **2021**, *33*, 2102271.
[38] C. Li, T. Hang, Y. Jin, *Exploration* **2023**, *3*, 20220151.
[39] L. Hu, H. Liao, L. Feng, M. Wang, W. Fu, *Anal. Chem.* **2018**, *90*, 6247.
[40] J. Zhang, W. Zheng, X. Jiang, *Small* **2018**, e1801680.
[41] H. Liao, G. Liu, Y. Liu, R. Li, W. Fu, L. Hu, *Chem. Commun. (Camb.)* **2017**, *53*, 10160.
[42] S. Romero-Garcia, J. S. Lopez-Gonzalez, J. L. B´Ez-Viveros, D. Aguilar-Cazares, H. Prado-Garcia, *Cancer Biol. Ther.* **2011**, *12*, 939.
[43] S. Guo, K. Li, B. Hu, C. Li, M. Zhang, A. Hussain, X. Wang, Q. Cheng, F. Yang, K. Ge, J. Zhang, J. Chang, X.-J. Liang, Y. Weng, Y. Huang, *Exploration (Beijing)* **2021**, *1*, 35.
[44] Y. Ding, Y. Wang, Q. Hu, *Exploration (Beijing)* **2022**, *2*, 20210106.
[45] C. De Gracia Lux, S. Joshi-Barr, T. Nguyen, E. Mahmoud, E. Schopf, N. Fomina, A. Almutairi, *J. Am. Chem. Soc.* **2012**, *134*, 15758.
[46] Y. Kirichok, G. Krapivinsky, D. E. Clapham, *Nature* **2004**, *427*, 360.
[47] K. J. Kamer, V. K. Mootha, *Nat. Rev. Mol. Cell Biol.* **2015**, *16*, 545.
[48] G. Van Loo, X. Saelens, M. Van Gurp, M. Macfarlane, S. J. Martin, P. Vandenabeele, *Cell Death Differ.* **2002**, *9*, 1031.
[49] D.-T. Lin, J. D. Lechleiter, *J. Biol. Chem.* **2002**, *277*, 31134.
[50] B. Yang, Y. Chen, J. Shi, *Adv. Mater.* **2019**, *31*, 1901778.
[51] M. Huo, L. Wang, Y. Wang, Y. Chen, J. Shi, *ACS Nano* **2019**, *13*, 2643.
[52] S.-Y. Li, H. Cheng, B.-R. Xie, W.-X. Qiu, J.-Y. Zeng, C.-X. Li, S.-S. Wan, L. Zhang, W.-L. Liu, X.-Z. Zhang, *ACS Nano* **2017**, *11*, 7006.
[53] C. Von Roemeling, W. Jiang, C. K. Chan, I. L. Weissman, B. Y. S. Kim, *Trends Biotechnol.* **2017**, *35*, 159.
[54] M. P. Murphy, H. Bayir, V. Belousov, C. J. Chang, K. J. A. Davies, M. J. Davies, T. P. Dick, T. Finkel, H. J. Forman, Y. Janssen-Heininger, D. Gems, V. E. Kagan, B. Kalyanaraman, N.-G. Larsson, G. L. Milne, T. Nyström, H. E. Poulsen, R. Radi, H. Van Remmen, P. T. Schumacker, P. J. Thornalley, S. Toyokuni, C. C. Winterbourn, H. Yin, B. Halliwell, *Nat. Metab.* **2022**, *4*, 651.